



Effect of helium ion irradiation on short-time corrosion behavior of two novel high-entropy alloys in simulated PWR primary water

Zijian Zhang ^{a,b}, En-Hou Han ^{a,*}, Chao Xiang ^{a,c}

^a Key Laboratory of Nuclear Materials and Safety Assessment, Institute of Metal Research, Chinese Academy of Sciences, Shenyang, 110016, China

^b School of Materials Science and Engineering, University of Science and Technology of China, Shenyang, 110016, China

^c Institute of Corrosion Science and Technology, Guangzhou, 510530, China



ARTICLE INFO

Keywords:

High-entropy alloys
High temperature corrosion
Irradiation
Oxide film

ABSTRACT

The effect of helium ion irradiation on the short-time corrosion behavior of two novel high-entropy alloys (HEAs) was investigated in simulated PWR primary water. The results revealed that a double-layer oxide film consisting of Ti, Nb and V oxides was formed on both HEAs, including outer oxide particles and a protective inner oxide layer with a maximum depth of ~500 nm. Irradiation up to 10.5 dpa may hardly promote corrosion kinetics since severe lattice distortion and sluggish diffusion in HEAs. The corrosion processes with and without irradiation were discussed in detail.

1. Introduction

High-entropy alloys (HEAs) composed of multiple major metallic elements, also called compositionally complex alloys (CCAs), were originally proposed by Yeh et al. [1] and Cantor et al. [2]. HEAs generally contain at least five prime elements in equimolar or near-equimolar ratio, and each element has an atomic concentration between 5 and 35 % [3,4]. In contrast to the conventional alloys, HEAs exhibit higher mixing entropy which may suppress the formation of ordered intermetallic compounds and favor the formation of a monophasic crystal structure instead. Due to the diversity of element selection, researchers can design numerous HEAs with desired properties such as mechanical property [5–7], thermal stability [8–10], wear resistance [11–13], corrosion resistance [14–16], and irradiation resistance [17–19]. It seems that to date studies have been primarily emphasized on the HEAs composed of transition metals such as Fe, Ni, Co, Cr and Mn. However, refractory high-entropy alloys (RHEAs) based on refractory elements have attracted less attention, while they may possess better properties at high temperature. For example, the CrNbTiVZr RHEA showed better high-temperature strength and higher melting point compared to Ni superalloys [20]. Gorr et al. [21–23] evaluated oxidation behaviors of three equimolar AlCrMoTi-X (X = Nb, W or Ta) RHEAs as well as the AlCrMoTiNb RHEA with minor additions of Si in air at 900–1100 °C, and all these RHEAs exhibited lower specific mass gains than commercial refractory alloys.

Corrosion is always a significant issue with the birth of new structural materials, particularly for metallic materials, because it can determine whether a promising material can be serviced in actual environments or not. With the rapid development of HEAs, corrosion of some HEAs has been systematically explored [14,15,24–29]. For instance, Lee et al. [24] investigated the effect of Al content on corrosion behavior of the $\text{Al}_x\text{CrFe}_{1.5}\text{MnNi}_{0.5}$ HEAs in aqueous environments. The addition of Al significantly affected the evolution of phase structures and reduced the resistance to pitting corrosion. Hsu et al. [29] studied the effect of Cu addition on corrosion behavior of the FeCoNiCrCu_x HEAs in a 3.5 wt.% NaCl solution. They found that the corrosion resistance of HEAs was generally decreased with the increase of the Cu concentration, and the HEAs without any Cu addition exhibited better pitting corrosion resistance than 304 L stainless steel. On the other hand, HEAs are characteristic of not only high value of entropy but also high atomic-level stresses originating from mixing of elements with different atomic sizes. Particle irradiation produces atomic displacements and thermal spikes. The high atomic-level stress in HEAs facilitates amorphization after irradiation, followed by local melting and re-crystallization due to thermal spikes [30], which will induce much fewer defects in HEAs than that in conventional alloys. For example, Yang et al. [18] reported that the CrMnFeCoNi HEAs possessed the most stable structure and the best helium ion irradiation resistance compared to the 304 stainless steel and pure Ni due to the fewest irradiation defects in HEAs.

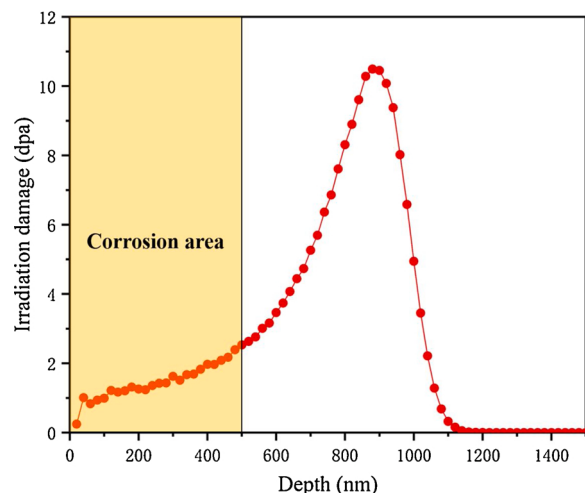
* Corresponding author.

E-mail address: ehhan@imr.ac.cn (E.-H. Han).

Table 1

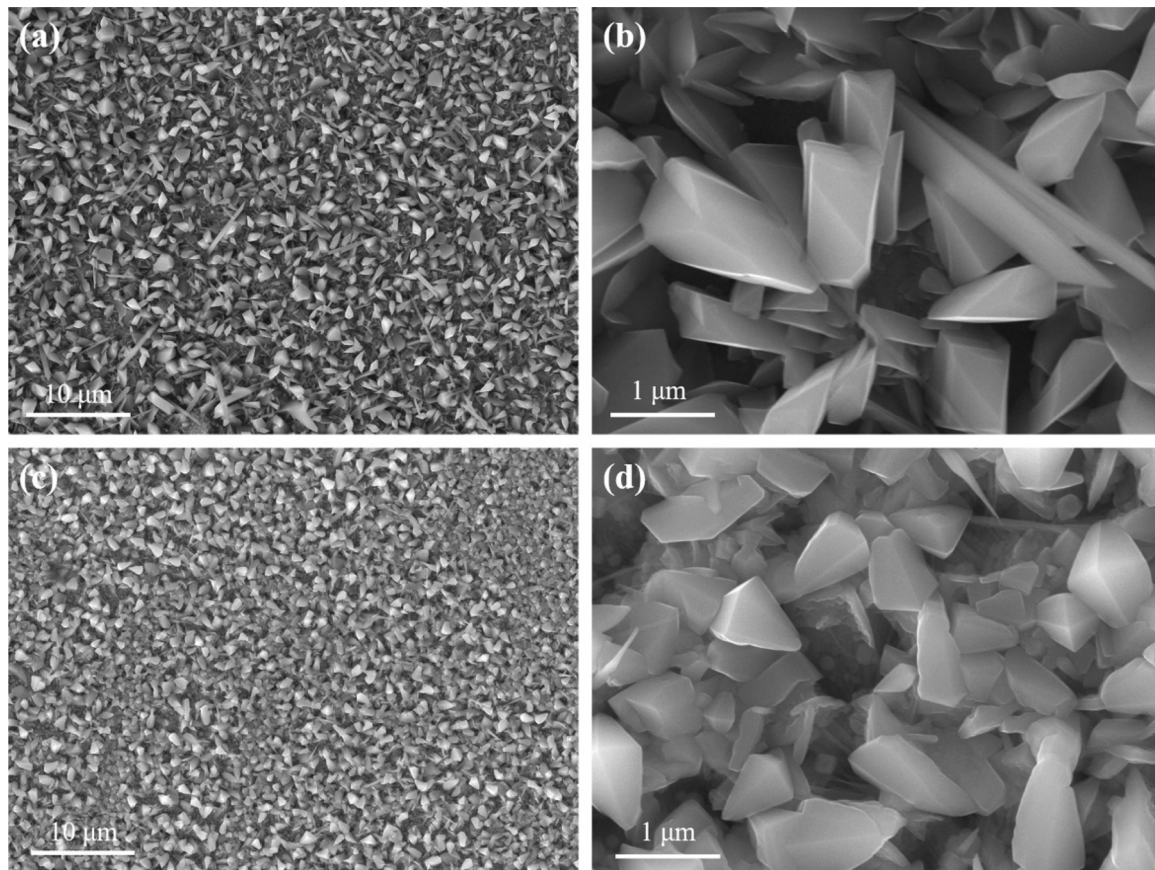
Nominal compositions (at.%) of the as-annealed Cr-HEA and Zr-HEA.

Alloy	Cr	Mo	Nb	Ti	V	Zr
Cr-HEA	6.66	13.33	26.67	26.67	26.67	–
Zr-HEA	–	15.38	30.77	30.77	15.38	7.70

**Fig. 1.** The depth damage profile as calculated by SRIM 2008 computer software.

The corrosion resistance and irradiation resistance provide HEAs with the promising capacity for nuclear power application in high temperature pressurized water environments. To date, there have been only several studies available on high temperature pressurized water corrosion of HEAs. Xiang et al. [31] compared the repassivation rate in high temperature pressurized water between three HEAs and 690 T T alloy, and they found that their repassivation rates followed the order of TaNbHfZrTi > Co_{1.5}CrFeNi_{1.5}Ti_{0.5}Mo_{0.1} > 690 T T > AlCoCrFeNiSi_{0.1}. Moreover, Liu et al. [32] investigated oxidation behaviors of the Al_x-CoCrFeNi ($x = 0.15, 0.4$) HEAs in supercritical water at 550 and 600 °C. When compared to the HR3C steel, the Al_xCoCrFeNi HEAs had a thinner oxide film and exhibited superior oxidation resistance to supercritical water. However, these reports about high temperature pressurized water corrosion of HEAs was insufficient for a comprehensive understanding of the corrosion process and mechanism of HEAs in high temperature pressurized water. Furthermore, the effect of irradiation on corrosion behavior of HEAs is unknown. Therefore, the corrosion of HEAs in high temperature pressurized water with and without irradiation should be urgently investigated.

Two novel Cr_{0.25}Mo_{0.5}NbTiV and Mo_{0.5}NbTiV_{0.5}Zr_{0.25} HEAs with low thermal neutron absorption cross-section elements were designed by our group for potential candidate material used as accident tolerant fuel cladding. Due to the neutron economy, the thermal neutron absorption cross-section of HEAs must be considered. Some works about mechanics and irradiation performance have been finished in our recent study [33,34]. In this work, the effect of irradiation on the short-time corrosion behaviors of the two HEAs was investigated, and then the corrosion processes with and without irradiation were discussed by a possible model. To our best knowledge, this is the first time to report the effect of irradiation on the corrosion behaviors of HEAs in high temperature pressurized water.

**Fig. 2.** SEM observation of the surface morphology of oxide films formed on the as-annealed Cr-HEA and Zr-HEA subjected to 200-h exposure in simulated PWR primary water at 320 °C. (a), (b) as-annealed Cr-HEA; (c), (d) as-annealed Zr-HEA.

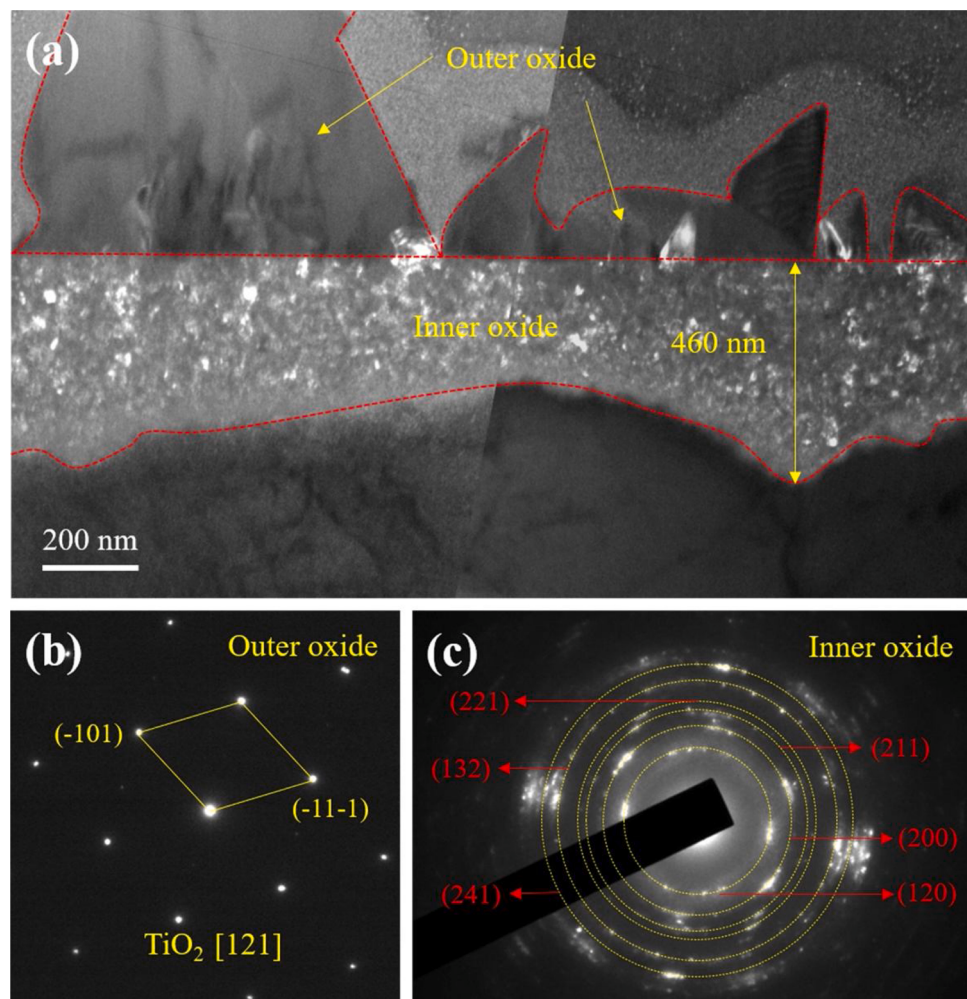


Fig. 3. (a) TEM observation of the cross-section of oxide film formed on the as-annealed Cr-HEA. SAED patterns of the outer oxide particle (b) and inner oxide layer (c).

2. Experimental

2.1. Material

The Mo_{0.5}NbTiVCr_{0.25} and Mo_{0.5}NbTiV_{0.5}Zr_{0.25} alloy ingots were fabricated by melting commercially pure metals (higher than 99.5 wt.%) in a water-cooled copper crucible of vacuum arc furnace under Ti-gittered argon atmosphere. For convenience, the two alloys are designated as Cr-HEA and Zr-HEA, respectively. These ingots were flipped over and remelted more than five times to ensure alloy homogenization. All ingots were hot isostatic pressed at 1200 °C and 150 MPa for 2 h to reduce the solidification porosity, followed by annealing treatment at 1200 °C for 72 h (Cr-HEA) or 24 h (Zr-HEA) under high purity argon flow. The nominal compositions of the Cr-HEA and Zr-HEA are shown in Table 1. According to our previous study [34], the two HEAs both have an equiaxed microstructure with a grain size of 100–200 μm and a single bcc structure.

2.2. Helium ion irradiation

Specimens with a dimension of 7 mm × 7 mm × 1 mm were cut from the central parts of the alloy ingots. Before helium ion irradiation, the specimens were ground using SiC papers from 120 grit up to 3000 grit, then mechanically polished using diamond pastes of 1.5 μm and 0.5 μm in turns, and lastly manually polished by 40-nm colloidal silica slurry for over 2 h to move the residual strain. All the irradiation experiments were

carried out at the 320 kV platform for multi-discipline research with highly charged ions at the Institute of Modern Physics, Chinese Academy of Sciences. The specimens were irradiated with 400 keV He²⁺ at 350 °C for 25 h. The damage peak doses are approximate 10.5 dpa at 900 nm, and the irradiation damage extends to a maximum depth of ~1100 nm. In addition, the maximum corrosion depth is ~500 nm in this study. The depth damage profile was calculated by the Stopping and Range of Ions in Materials 2008 (SRIM 2008) software, and the corrosion area was marked, as shown in Fig. 1.

2.3. Exposure test

The exposure tests were conducted at 320 °C in simulated PWR primary water in an autoclave, which is equipped with a refreshed water loop. The water contained 1200 mg/L of B as H₃BO₃ and 2.3 mg/L of Li as LiOH, with a dissolved hydrogen (DH) concentration of 2.6 mg/L. The DH was achieved by applying a hydrogen overpressure of 0.08 MPa in the water tank of the loop after removal of air in the water by bubbling hydrogen. To study the effect of irradiation on corrosion behavior, both the as-annealed and irradiated specimens were exposed to the water with a fixed exposure of 200 h.

2.4. Analysis of the oxide film

After the exposure tests, the specimens were removed from the autoclave and cleaned with deionized water for characterization of the

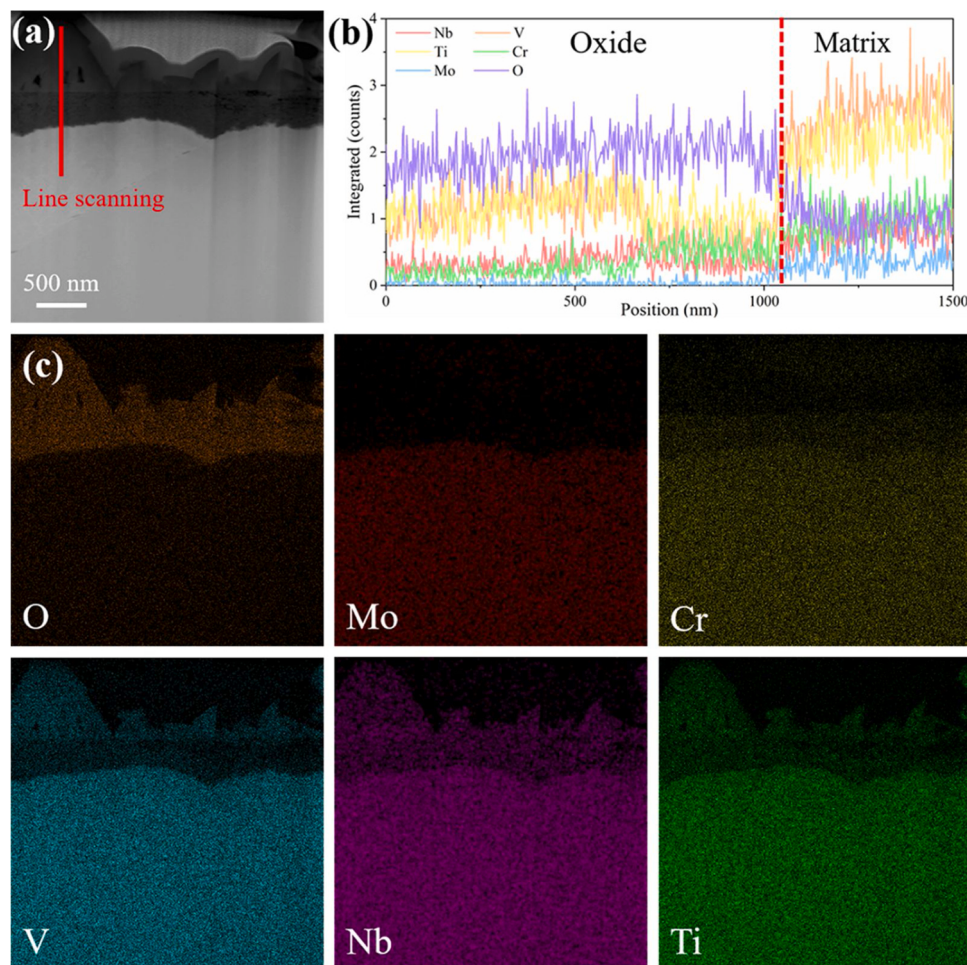


Fig. 4. (a) STEM image of the cross-section of oxide film formed on the as-annealed Cr-HEA. (b) EDX line scanning along red line. (c) The corresponding element mappings of O, Cr, V, Ti, Mo, Nb. (For interpretation of the references to colour in this figure legend, the reader is referred to the web version of this article).

oxide film. The surface morphology of the oxide film was studied by using a FEI XL30 Field Emission Gun scanning electron microscope (SEM). The microstructure of the oxide film was examined by using a JEM-2100 F transmission electron microscope (TEM) at 200 kV equipped with an energy dispersive X-ray spectroscope (EDX). During TEM observation, selected area electron diffraction (SAED) was used to identify the crystalline structure of the oxide film, while EDX mapping was used to analyze the chemical composition of the oxide film. The TEM specimens of the cross-section of the oxide film were prepared by a Helios 600i focused ion beam (FIB), which can vertically lift out the specific volumes containing the oxide film and matrix by the Ga-ion beam.

3. Results

3.1. Surface morphology of oxide film formed on as-annealed HEAs

SEM observation of the oxide films formed on the as-annealed HEAs after exposure test is shown in Fig. 2. The oxide films of both Cr-HEA and Zr-HEA consist of polyhedral oxide particles and needle-like oxides. However, the particle size and needle length of Zr-HEA are relatively smaller compared to Cr-HEA. It is difficult to observe the underneath oxide film under SEM since the specimen surface is almost entirely covered by the dense oxide particles. Precise TEM analyses of the structure and composition of the underneath oxide film from the cross-section are described in the following section.

3.2. Cross-sectional analysis of the oxide film of as-annealed HEAs

A detailed cross-sectional analysis was performed since the inner oxide layer was mostly covered by the oxide particles. Fig. 3 shows TEM observation of the cross-section of the oxide film formed on the as-annealed Cr-HEA. The oxide film with a double-layer structure is observed in Fig. 3a, which is composed of an outer oxide layer of polyhedral oxide particles and a continuous inner oxide layer with a maximum thickness of ~460 nm. In addition, the SAED patterns obtained from the outer oxide particle and the inner oxide layer (Fig. 3b and c) exhibit monocrystal and polycrystal features, respectively. Fig. 4 shows the image under scanning transmission electron microscopy (STEM) mode and the corresponding element mappings of the cross-sectional oxide film formed on the Cr-HEA, together with the EDX line scanning profile from oxide to matrix. The outer oxide particle is primarily composed of V, Ti and Nb oxides, while the inner oxide layer mainly consists of Nb and Ti oxides.

Similar to the Cr-HEA, the corrosion product of the Zr-HEA also exhibits a double-layer oxide structure, which consists of polyhedral oxide particles and a continuous inner oxide layer with a maximum corrosion depth of ~530 nm, as shown in Fig. 5a. SAED patterns in Fig. 5b and c indicate a monocrystal structure for the outer layer and a polycrystal structure for the inner layer, respectively. Fig. 6 shows STEM image and the corresponding element mappings of the oxide film of the Zr-HEA, as well as the EDX line scanning profile from oxide to matrix. Both the outer oxide particles and inner oxide layer mainly consist of V and Ti oxides. The chemical compositions of the outer oxide particles and inner

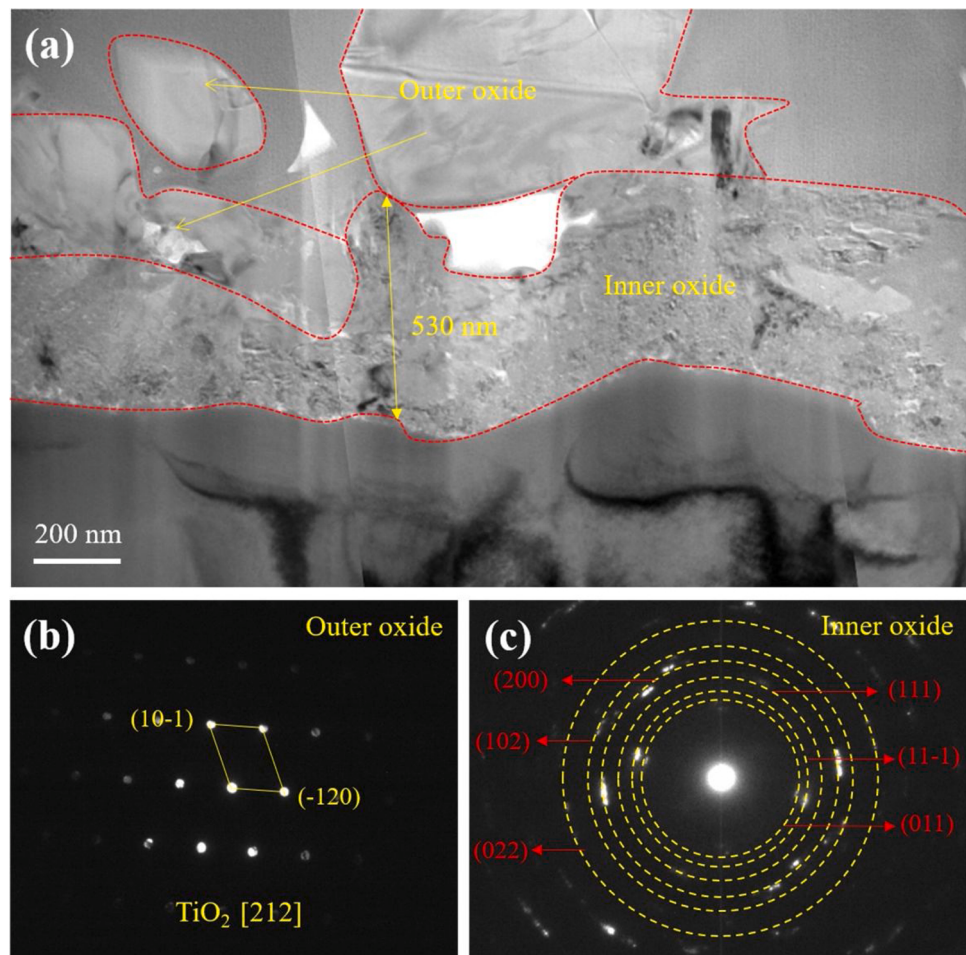


Fig. 5. (a) TEM observation of the cross-section of oxide film formed on the as-annealed Zr-HEA. SAED patterns of the outer oxide particle (b) and inner oxide layer (c).

oxide layer formed on the as-annealed Cr-HEA and Zr-HEA are listed in Table 2, indicating the oxide film of the two HEAs mainly consists of three component elements of Ti, V and Nb.

Fig. 7 shows the high-magnification TEM observations of oxide scales of the two as-annealed HEAs. The TEM bright-field observations of the outer oxide particles exhibit a monocrystal morphology, while the high-magnification TEM observations of the inner oxide layer reveal a nanocrystal structure. These results are consistent with the SAED patterns of the oxides in Figs. 3 and 5. To our best knowledge, there are very few reports available about the structure of oxide scale formed on HEAs in high temperature pressurized water. Chen et al. [35] studied selected corrosion behaviors of Cu_{0.5}NiAlCoCrFeSi bulk glassy alloy in 288°C high-purity water, and they found that the oxide film mainly consisted of three layers including monocrystal outer layer and polycrystal middle layer and inner layer.

3.3. Short-time corrosion behaviors of irradiated HEAs

As shown in Fig. 8, two types of defects including helium bubbles (1–3 nm in size) and dislocation loops (4–6 nm in size) are observed, which has been detailed in our previous study [34]. The irradiation defects in the HEAs studied in this work appear to have a smaller size than that of the conventional alloys like stainless steel under a similar irradiation condition [36–39]. SEM observation of the surface morphology of oxide films formed on the irradiated HEAs is shown in Fig. 9. It can be found that the oxide films of these two irradiated HEAs both consist of polyhedral oxides and needle-like oxides like the as-annealed HEAs.

The cross-sectional TEM observation of oxide films formed on the irradiated Cr-HEA and Zr-HEA is showed in Fig. 10. The maximum corrosion depth of the irradiated Cr-HEA reaches ~460 nm, which is substantially the same as the as-annealed Cr-HEA (~460 nm) and still within the depth range of irradiation damage. However, it is noted that the irradiated Zr-HEA has a maximum corrosion depth of ~420 nm, and is smaller than the oxide thickness of the as-annealed Zr-HEA (~530 nm). This result suggests that the irradiation appears to have no obvious effect on the corrosion kinetics of Cr-HEA but reduce the corrosion kinetics of Zr-HEA. Analyses of crystalline structure and chemical composition of the oxide films formed on the irradiated Cr-HEA and Zr-HEA are shown in Figs. 11 and 12, respectively. According to the STEM images (Figs. 11a and 12 a and the corresponding element mappings (Figs. 11d and 12 d), both the irradiated Cr-HEA and Zr-HEA have a double-layer oxide mainly consisting of V, Ti and Nb oxides. Figs. 11b–c and 12 b–c show the SAED patterns of the outer oxide particle and inner oxide layer of the irradiated Cr-HEA and Zr-HEA, respectively. Like the as-annealed HEAs, the outer oxide particles of both irradiated HEAs also show a monocrystal structure, and the inner oxide layer remains a polycrystal structure. According to these results, there are no obvious microstructural and microchemical changes induced by irradiation for the two HEAs.

4. Discussion

4.1. Corrosion mechanism of the as-annealed HEAs

As mentioned earlier, the TEM observations (Figs. 3 and 5) indicate

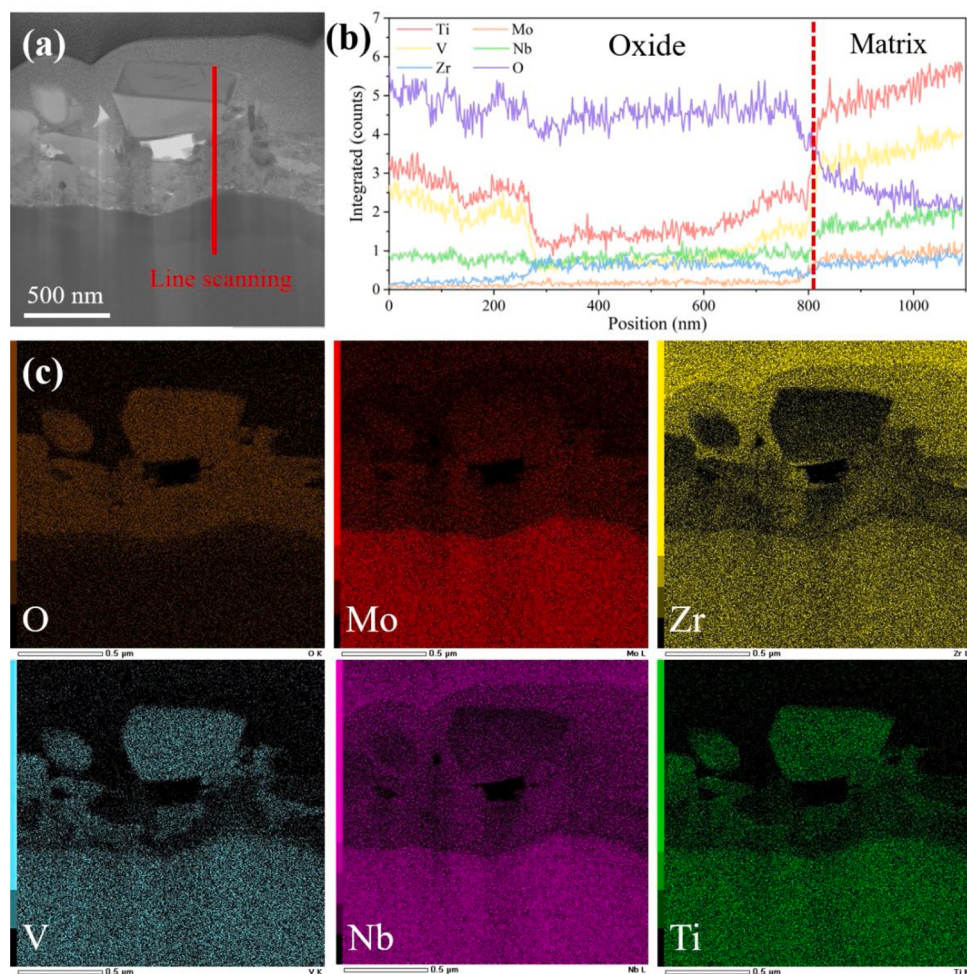


Fig. 6. (a) STEM image of the cross-section of oxide film formed on the as-annealed Zr-HEA. (b) EDX line scanning along red line. (c) The corresponding element mappings of O, Zr, V, Ti, Mo, Nb. (For interpretation of the references to colour in this figure legend, the reader is referred to the web version of this article).

Table 2

Chemical compositions (at.%) of the outer oxide particles, inner oxide layer and base metal in the as-annealed Cr-HEA and Zr-HEA.

Alloy	Position	O	Cr	Mo	Nb	Ti	V	Zr
Cr-HEA	outer	55.66	0.57	0	12.80	16.99	13.98	–
	inner	58.82	6.93	0	12.93	14.11	7.21	–
	metal	–	6.61	14.14	27.14	26.29	25.82	–
Zr-HEA	outer	56.94	–	0.16	14.98	16.38	9.90	1.64
	inner	59.94	–	0	13.55	14.50	8.17	3.85
	metal	–	–	16.97	29.96	29.42	14.19	9.46

that the as-annealed Cr-HEA and Zr-HEA both possess a double-layer oxide structure including outer oxide particles and a continuous inner oxide layer. By combining the SAED patterns (Figs. 3 and 5) with chemical compositions (Table 2) of the oxide films, the outer oxide particles of two HEAs consist of TiO_2 , while the inner oxide layer is primarily composed of nanocrystalline TiO_2 .

Table 3 shows the electronegativity of all component elements in Cr-HEA and Zr-HEA, which follows the order of $\text{Zr} < \text{Ti} < \text{Nb} < \text{V} < \text{Cr} < \text{Mo}$. The element with lower electronegativity is more likely to react with oxygen. Moreover, Gibbs free energy of oxide can also be used to evaluate the affinity of the elements above with oxygen, and the oxide with lower Gibbs free energy will be easier to form. Table 4 lists the Gibbs free energy of oxides corresponding to the component elements contained in two HEAs, which was calculated by using the free energy function method. For a clear comparison, only the oxide with the minimum Gibbs free energy for each element is included. The Zr oxide has

the lowest Gibbs free energy, followed by the Ti oxide. Therefore, oxidation of Zr may preferentially occur over Ti due to either the lower electronegativity or the smaller Gibbs free energy of Zr with comparison to Ti. Nevertheless, since the concentration of Ti is the highest in the Cr-HEA and nearly four times as high as the concentration of Zr in the Zr-HEA, Ti oxides are most likely to form in both the Cr-HEA and Zr-HEA.

The two HEAs have similar corrosion behaviors in terms of the oxide composition, double-layer structure, and thickness of the oxide film. Therefore, only formation mechanism of the oxide film of Cr-HEA is discussed. The oxide films with the double-layer structure have been commonly reported in conventional alloys such as Fe-Cr-Ni alloys after exposure to high temperature pressurized water [40–43]. It is known that the inner oxide layer grows by the oxidation of the metal following the ingress of oxidants along micropores in the oxide, while the outer layer grows by the outward diffusion of metal cations through the oxide film. Due to the difference in diffusion rate of component elements in

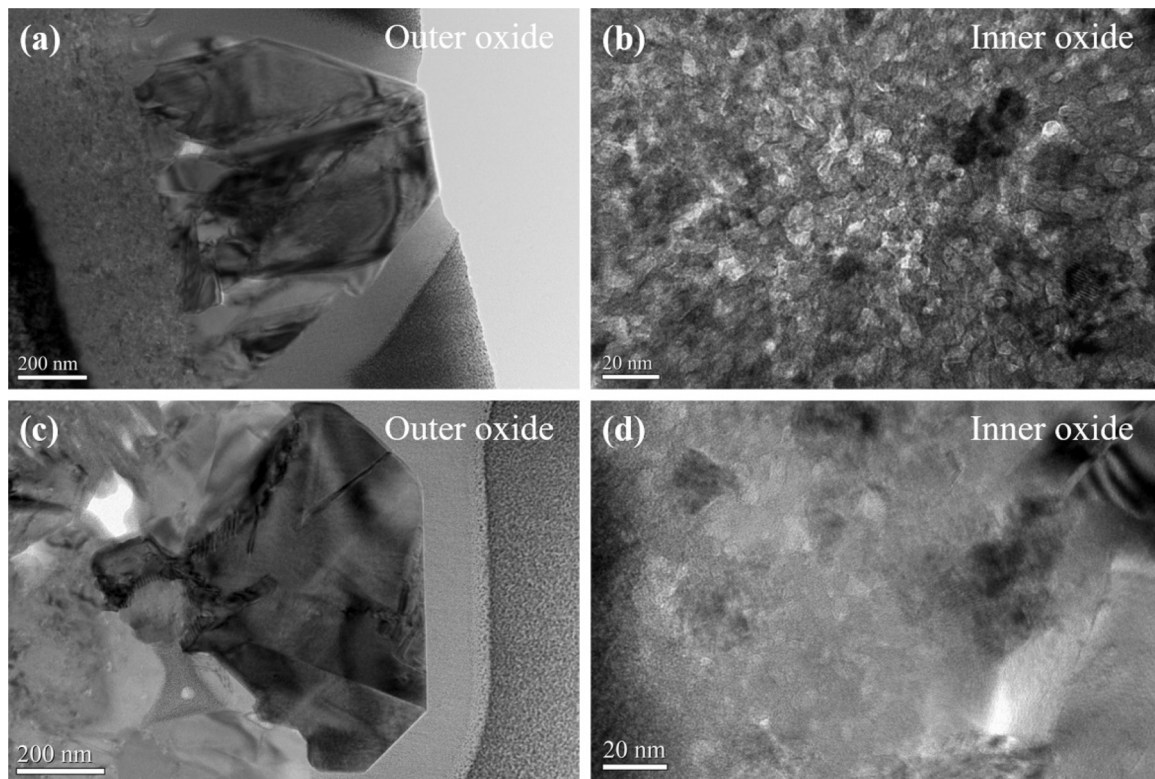


Fig. 7. High-magnification TEM observation of oxide films formed on the two as-annealed HEAs. Outer oxide particles (a) and inner oxide layer (b) of the Cr-HEA; Outer oxide particles (c) and inner oxide layer (d) of the Zr-HEA.

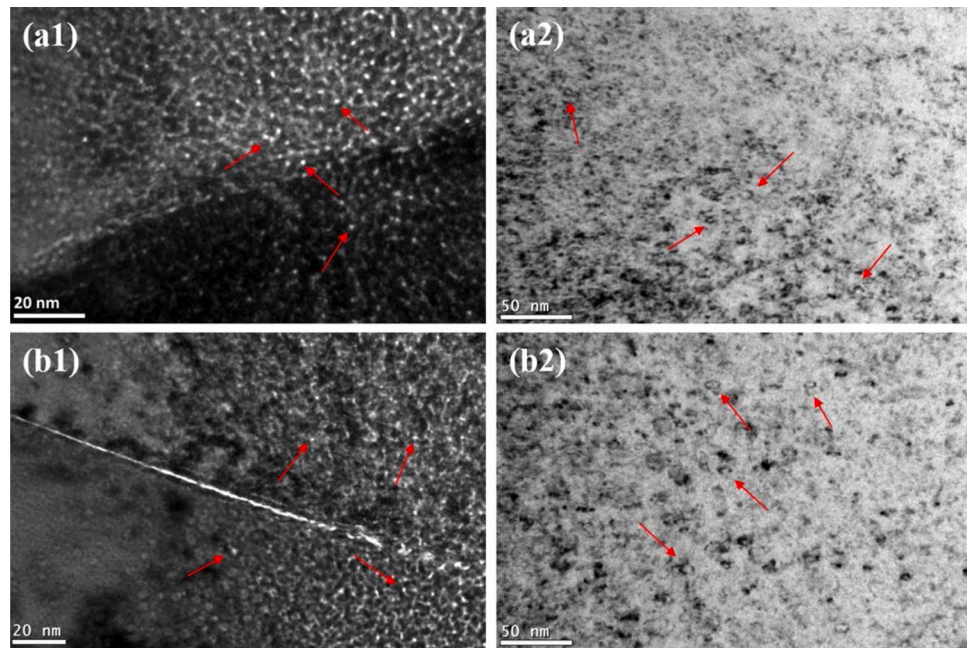


Fig. 8. TEM observation of defects induced by helium ion irradiation of 10.5 dpa. Helium bubbles (a1) and dislocation loops (a2) in irradiated Cr-HEA; Helium bubbles (b1) and dislocation loops (b2) in irradiated Zr-HEA. Some irradiation defects are marked by red arrows. (For interpretation of the references to colour in this figure legend, the reader is referred to the web version of this article).

Fe-Cr-Ni alloys ($\text{Fe} > \text{Ni} > \text{Cr}$), the inner layer is typically enriched in Cr while the outer layer is generally enriched in Fe and Ni [41]. However, in this work, similar chemical compositions were found between the inner layer and outer particles formed on the Cr-HEA. This implies that the Cr-HEA may have a different corrosion mechanism from that of

Fe-Cr-Ni alloys. According to the corrosion results of Cr-HEA and the existing models for corrosion mechanism of Fe-Cr-Ni alloys in high temperature pressurized water, the corrosion mechanism of the Cr-HEA is proposed in the present work.

According to the electronegativity of metal species with the order of

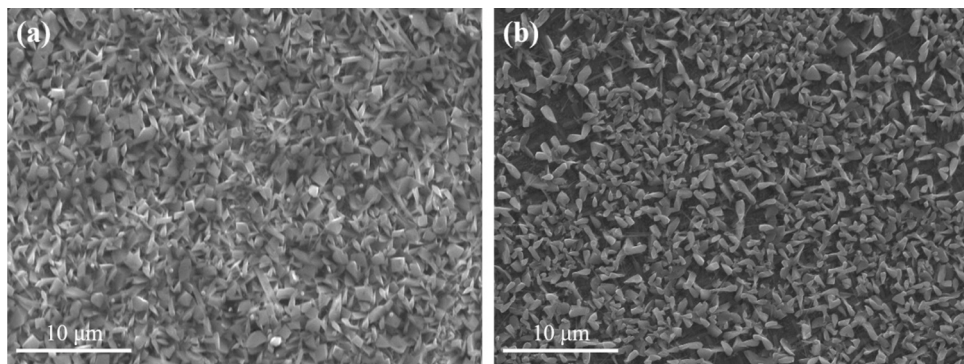


Fig. 9. SEM observation of the surface morphology of oxide films formed on the irradiated Cr-HEA (a) and Zr-HEA (b).

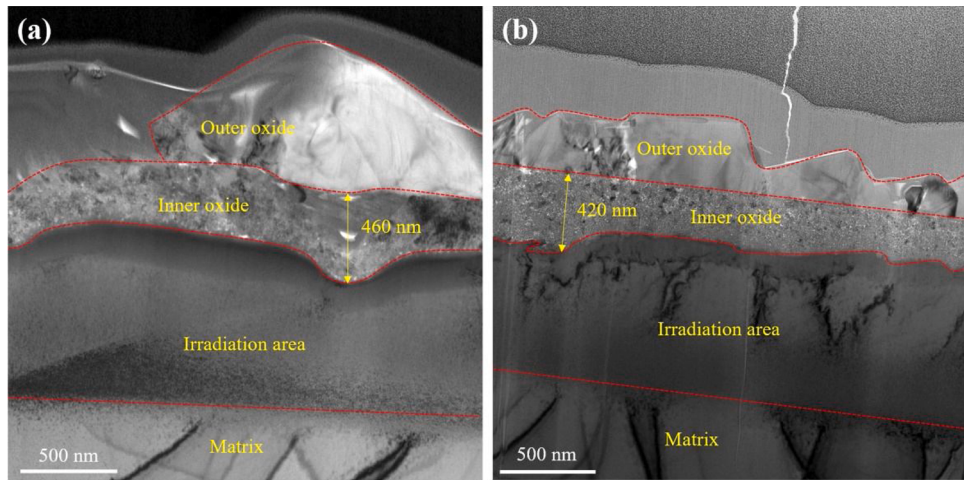
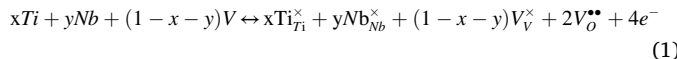


Fig. 10. The cross-sectional TEM observation of oxide films formed on the irradiated Cr-HEA (a) and Zr-HEA (b).

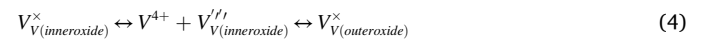
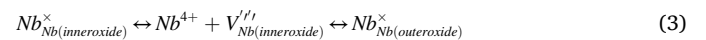
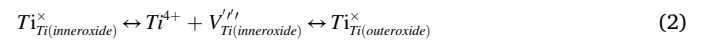
$Ti < Nb < V < Cr < Mo$, the oxidation of Ti would preferentially occur over the other elements. As the oxygen diffuses inwards, the Ti is oxidized to form TiO_2 at oxide/matrix interface. With the consumption of Ti element, the local Ti concentration at the oxide/matrix interface will be insufficient due to the sluggish diffusion of Ti in HEAs. As a result, the Nb and V elements are subsequently oxidized to form $(Ti, Nb, V)O_2$ by replacing the cation site of Ti. According to the point-defect mechanism [44,45], the transformation from metal atoms into cations can be described by the reaction (1) at the oxide/matrix interface:



where Ti, Nb and V indicate the metal atoms in the matrix, Ti_{Ti}^x , Nb_{Nb}^x and V_V^x indicate the metal cations in cation site in the inner oxide layer, $V_O^{2\bullet}$ indicates the oxygen vacancy, and e^- indicates the electron. The oxygen diffuses toward the oxide/matrix interface (or $V_O^{2\bullet}$ toward the outer surface), leading to the continuous inward migration of the oxide/matrix interface. The diffusion of oxygen vacancies and cations plays a role in the inner oxide growth. The severe lattice distortion in the Cr-HEA provides obstacles to the diffusion of metal atoms, which can suppress the growth process but promote the nucleation process of the inner oxide. Therefore, the inner oxide layer exhibits a fine-grained structure, as shown in the TEM observation of the inner oxide of the Cr-HEA in Fig. 7b.

According to the dissolution and redeposition mechanism [40,44] for Fe-Cr-Ni alloys, the Fe and Ni will diffuse into the water medium or interact with the absorbed H_2O to finally precipitate the oxide particles due to their faster diffusion rate in the inner oxide than Cr. For the

Cr-HEA, however, metal atoms can hardly pass through the inner layer to form the outer oxide particles. Therefore, the formation of outer particles may be caused by the dissolution and redeposition of the metal cations in the inner layer near the water medium, which can be described by the reactions (2) through (4):



where $Ti_{Ti(inneroxide)}^x$, $Nb_{Nb(inneroxide)}^x$ and $V_{V(inneroxide)}^x$ indicate the metal cations in cation site in the inner oxide layer, Ti^{4+} , Nb^{4+} and V^{4+} indicate the metal cations in the solution, $V_{Ti(inneroxide)}^{''/'}$, $V_{Nb(inneroxide)}^{''/'}$ and $V_{V(inneroxide)}^{''/'}$ indicate the metal vacancies in the inner oxide layer, and $Ti_{Ti(outeroxide)}^x$, $Nb_{Nb(outeroxide)}^x$ and $V_{V(outeroxide)}^x$ indicate the metal cations in cation site in the outer oxide particles. Therefore, the dissolution and redeposition of cations in the inner oxide play a role in the outer oxide growth.

The inner oxide layer grows by oxidation of the metal atoms following the inward diffusion of oxygen. The oxygen diffuses toward the oxide/matrix interface, leading to the continuous inward migration of the oxide/matrix interface. Then, the outer oxide particles grow by the dissolution and redeposition of the metal cations of the inner oxide layer near the water medium. The above processes, as well as those of Fe-Cr-Ni alloys, can be schematically depicted in Figs. 13a and 13b. The interfacial reaction (1) at outer oxide/inner oxide and reactions (2)–(4)

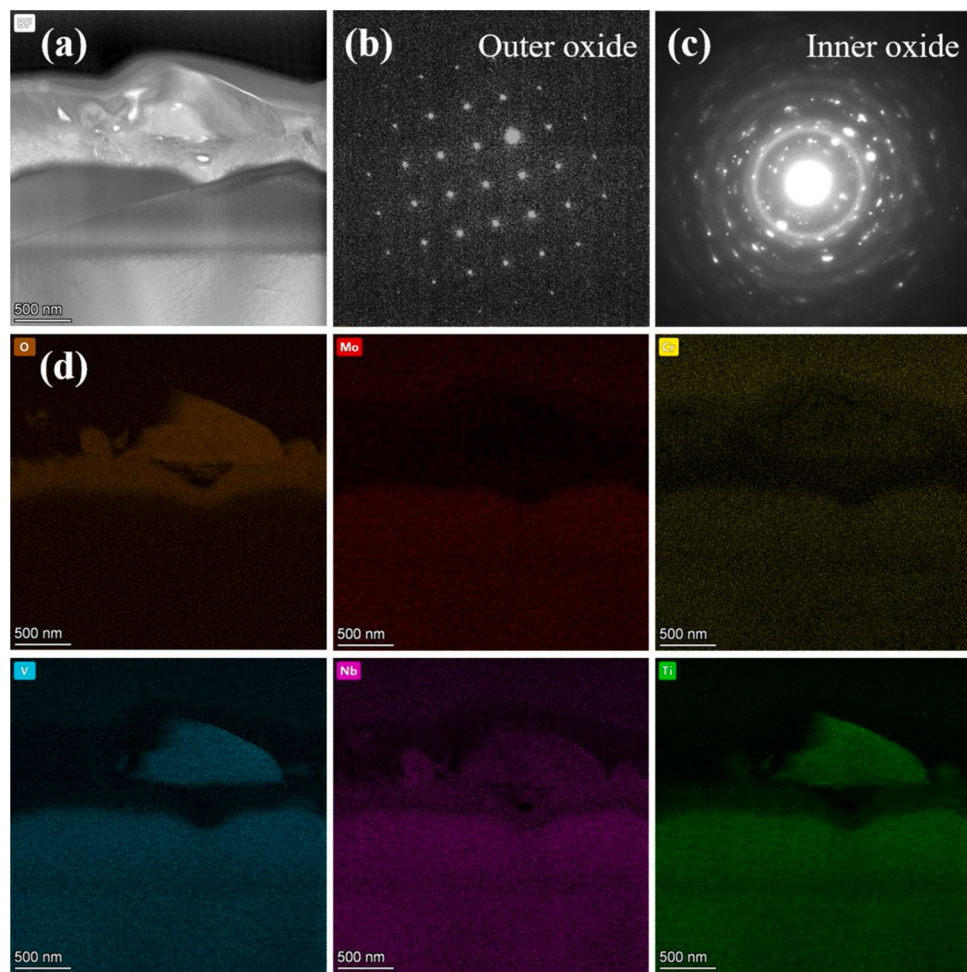


Fig. 11. (a) STEM bright-field image of the cross-section of oxide film formed on the irradiated Cr-HEA. SAED patterns of the outer oxide particle (b) and inner oxide layer (c) of the irradiated Cr-HEA. (d) The corresponding element mappings of O, Mo, Ti, V, Nb, Cr.

at inner oxide/matrix control the corrosion processes of Cr-HEA, and these reactions occur in a shorter range compared with Fe-Cr-Ni alloys.

There are some porosity-like defects in the inner oxide film (Fig. 10). Because the inward diffusion of oxygen in the HEAs is hindered, the local oxygen content of the oxide/matrix interface will be low as the corrosion proceed. This may cause the formation of polycrystal oxides at oxide/matrix interface. Some cations diffuse into solution, which can cause generation of cation vacancies at the oxide/matrix interface. The coalescence of these cation vacancies eventually results in the formation of pores in the inner layer as the corrosion proceeds. In addition, the cross-sectional samples were prepared by FIB including a procedure of Ga ions thinning. Since the inner layer consists of tiny nano-scale oxides, a part of them will sputter out due to the bombardment of Ga ions, resulting in porosity-like defects in the inner oxide film. However, in comparison with zirconium alloys which have a thick oxide film with many pores and microcracks [46–48], the HEAs show better corrosion resistance in high temperature water. Furthermore, Ti and Nb are beneficial to forming highly protective oxide film according to references [49,50]. The Ni-rich zones are usually observed at the oxide/matrix interface of Fe-Cr-Ni alloys, which is attributed to selective oxidation of Cr and rejection against Ni [51,52]. The local composition difference of matrix can influence corrosion. For example, the Cr-depleted zone can increase the intergranular corrosion susceptibility of the aged stainless steels [53]. However, no trace of the element-rich zone is observed in the two HEAs, indicating that the chemical composition of the matrix near the oxide/matrix interface can remain stable. The Cr-HEA exhibits special corrosion behaviors compared to the conventional alloys, possessing

better corrosion resistance than zirconium alloys in high temperature pressurized water.

4.2. Effect of irradiation on short-time corrosion behavior

To date, some studies about post-irradiation corrosion in high temperature pressurized water [54–58] have received increasing attention. Perrin et al. [55] reported that the irradiated 316 L stainless steel formed a thinner inner film compared with the unirradiated one. In contrast, Deng et al. [54] indicated that irradiation considerably promoted intergranular corrosion of 304NG stainless steel. The irradiation assisted corrosion in stainless steel is likely attributed to irradiation induced structure defects and element segregation, which can enhance the general corrosion and intergranular local corrosion, respectively. In this study, irradiation has little influence on composition and structure of the oxide films of the Cr-HEA. Furthermore, the thickness of the inner oxide film remains almost unchanged, indicating that irradiation can hardly assist corrosion of the Cr-HEA in high temperature pressurized water.

It is known that irradiation can induce a large number of defect clusters, dislocation loops, voids, bubbles and precipitates in Fe-Cr-Ni alloys [39,59], resulting in degradation of corrosion resistance. However, only dislocation loops and bubbles are observed in the two HEAs. Such defects with a small size (Fig. 8) in HEAs have little effect on enhancing the diffusion of oxygen and metal atoms. Moreover, the short-term diffusion in Cr-HEA is hard to be enhanced by defects, because the metal atoms in Cr-HEA have fewer probabilities to react with defects during a short-term migration. Therefore, the corrosion

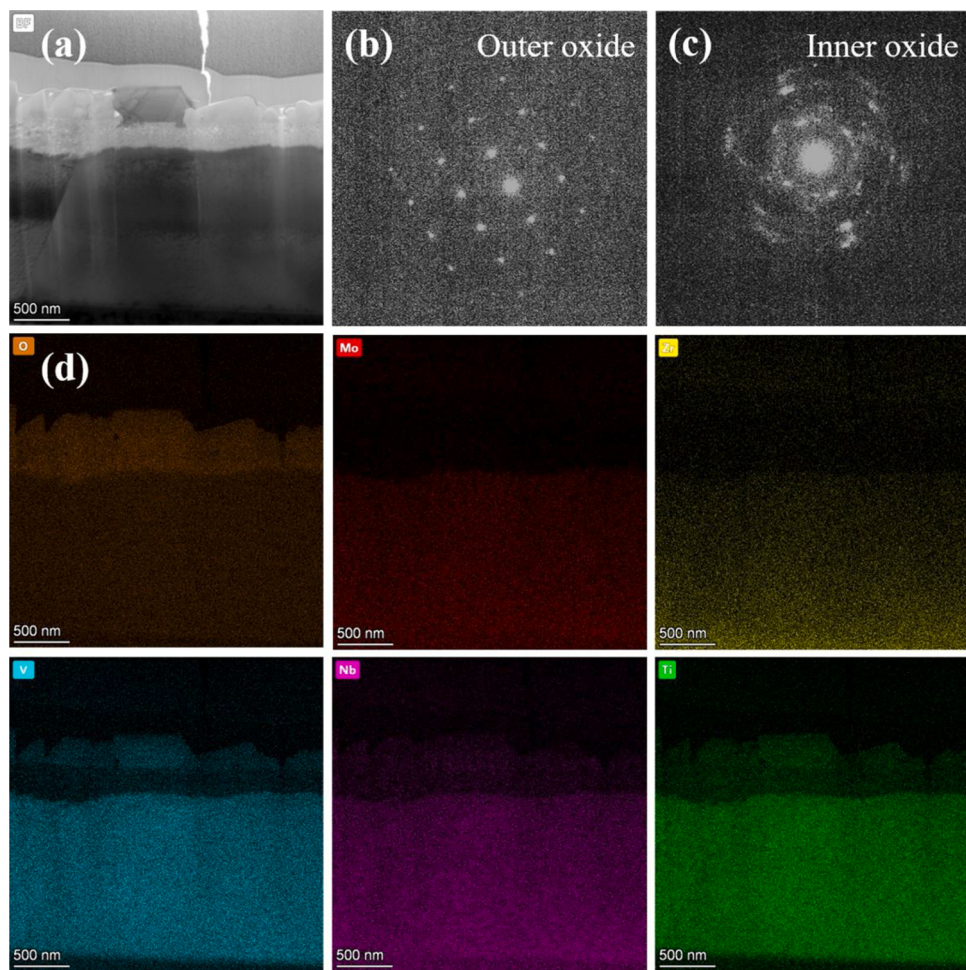


Fig. 12. (a) STEM bright-field image of the cross-section of oxide film formed on the irradiated Zr-HEA. SAED patterns of the outer oxide particle (b) and inner oxide layer (c) of the irradiated Zr-HEA. (d) The corresponding element mappings of O, Mo, Ti, V, Nb, Zr.

Table 3
Electronegativity of component elements in the Cr-HEA and Zr-HEA.

Element	Cr	Mo	Nb	Ti	V	Zr
Electronegativity	1.66	2.16	1.60	1.54	1.63	1.33

behavior of the Cr-HEA may be nearly unaffected by the irradiation unlike Fe-Cr-Ni alloys. The corrosion processes of the irradiated Fe-Cr-Ni alloys and Cr-HEA as discussed above are schematically shown in Fig. 13c and d.

As mentioned above, the Cr-HEA forms compact oxide film consisting of Ti, Nb and V oxides, and irradiation has little influence on corrosion processes. Therefore, the Cr-HEA may be suitable to the environment of high temperature pressurized water and irradiation. The Zr-HEA has similar corrosion behavior with the Cr-HEA in as-annealed and irradiated conditions. Besides, the thickness of the oxide film of Zr-HEA even reduces after irradiation. This result that irradiation reduces corrosion was also found in Zr-Nb alloys containing from 1 to 2.5 % of Nb [60] since the Nb played a role in rate reduction of corrosion under irradiation. In summary, irradiation up to 10.5 dpa may hardly

enhance high temperature pressurized water corrosion of both HEAs, which implies a potential implication of these two HEAs to nuclear materials.

5. Conclusions

The short-time corrosion behaviors in simulated PWR water environment were investigated on two novel HEAs under as-annealed and helium-irradiated conditions. The following conclusions can be drawn from this investigation:

- (1) The two as-annealed HEAs show a double-layer oxide film, which is composed of V, Ti and Nb oxides.
- (2) The inner oxide grows by oxidation of the metal atoms following the inward diffusion of oxygen, while the outer oxide particles grow by the dissolution and redeposition of the metal cations in the inner layer near the water medium.
- (3) The HEAs have a more protective oxide film compared with zirconium alloys according to literature.
- (4) Helium ion irradiation can hardly enhance the corrosion kinetics of both HEAs in high temperature pressurized water, which may

Table 4
Summary of the oxides with minimal Gibbs free energy ($\text{J}\cdot\text{mol}^{-1}\text{ K}^{-1}$) for each component element in the Cr-HEA and Zr-HEA.

Oxide	Cr_2O_3	MoO_2	NbO	TiO	VO	ZrO_2
Gibbs free energy	-644937	-403883	-711816	-941450	-752684	-981956

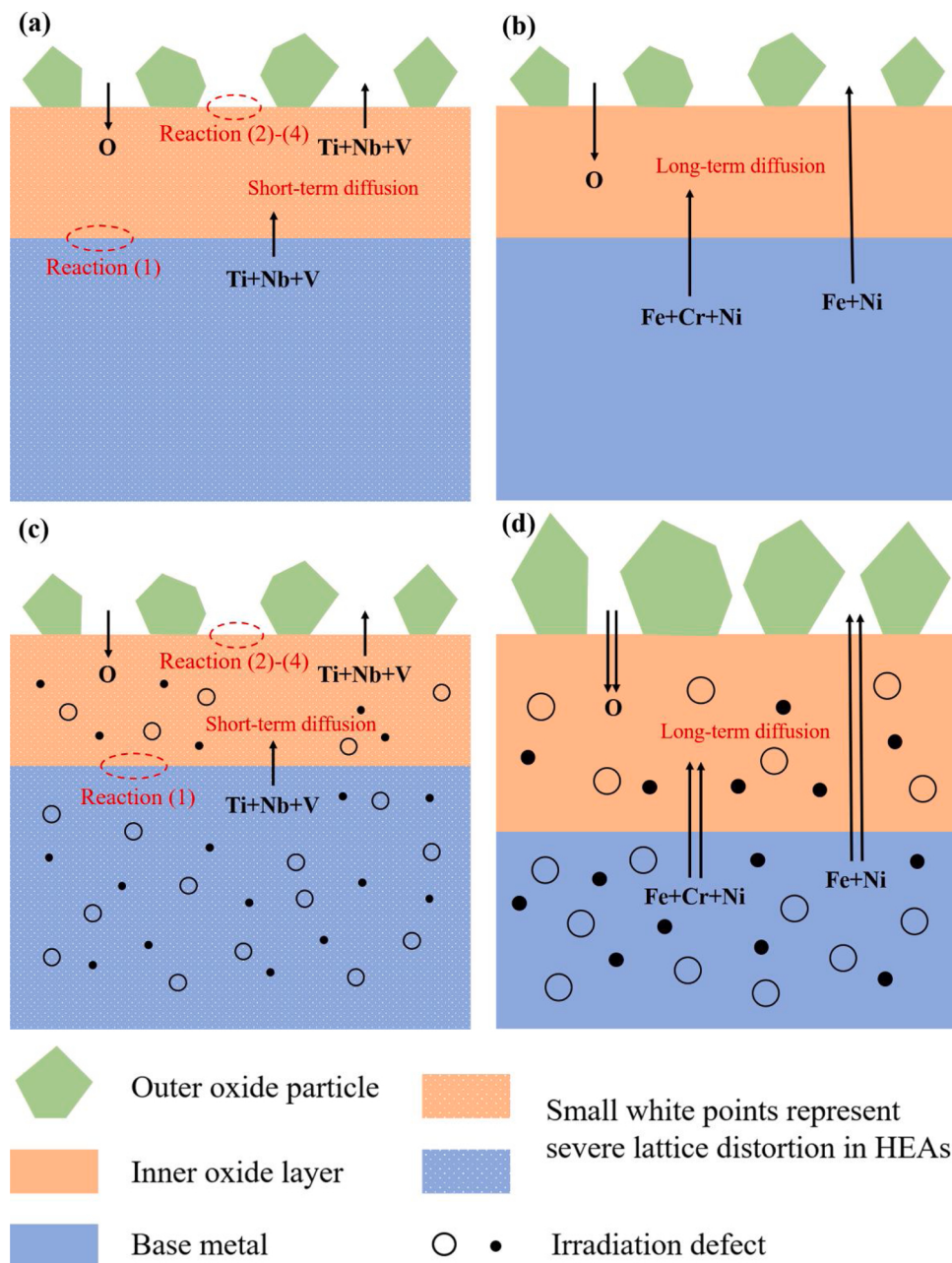


Fig. 13. Schematic of the corrosion processes of alloys exposed to high temperature water. Cr-HEA (a) and Fe-Cr-Ni alloy (b) before irradiation; Cr-HEA (c) and Fe-Cr-Ni alloy (d) after irradiation.

be attributed to the severe lattice distortion and sluggish diffusion of metal atoms in HEAs.

Author statement

Zijian Zhang: Conceptualization, Methodology, Investigation, Data Curation, Formal analysis, Writing - Original Draft.

En-Hou Han: Writing - Review & Editing, Visualization, Funding acquisition, Project administration, Supervision.

Chao Xiang: Resources, Writing - Review & Editing.

Declaration of Competing Interest

The authors declare that they have no known competing financial interests or personal relationships that could have appeared to influence the work reported in this paper.

Acknowledgement

This work was supported by the LingChuang Research Project of China National Nuclear Corporation. The authors are grateful to Xue Liang, Xiaodong Lin and Yifeng Li for their assistance to perform the FIB and TEM analyses.

References

- [1] J.W. Yeh, S.K. Chen, S.J. Lin, J.Y. Gan, T.S. Chin, T.T. Shun, C.H. Tsau, S.Y. Chang, Nanostructured high-entropy alloys with multiple principal elements: novel alloy design concepts and outcomes, *Adv. Eng. Mater.* 6 (2004) 299–303.
- [2] B. Cantor, I.T.H. Chang, P. Knight, A.J.B. Vincent, Microstructural development in equiatomic multicomponent alloys, *Mater. Sci. Eng. A* 375-377 (2004) 213–218.
- [3] Y. Zhang, T.T. Zuo, Z. Tang, M.C. Gao, K.A. Dahmen, P.K. Liaw, Z.P. Lu, Microstructures and properties of high-entropy alloys, *Prog. Mater. Sci.* 61 (2014) 1–93.

- [4] W. Zhang, P.K. Liaw, Y. Zhang, Science and technology in high-entropy alloys, *Sci. China Mater.* 61 (2018) 2–22.
- [5] B. Gludovatz, A. Hohenwarter, D. Catoor, E.H. Chang, E.P. George, R.O. Ritchie, A fracture-resistant high-entropy alloy for cryogenic applications, *Science* 345 (2014) 1153–1158.
- [6] Y. Zou, H. Ma, R. Spolenak, Ultrastrong ductile and stable high-entropy alloys at small scales, *Nat. Commun.* 6 (2015) 7748.
- [7] O.N. Senkov, J.M. Scott, S.V. Senkova, D.B. Miracle, C.F. Woodward, Microstructure and room temperature properties of a high-entropy TaNbHfZrTi alloy, *J. Alloys Compd.* 509 (2011) 6043–6048.
- [8] F. Otto, A. Dlouhý, C. Somsen, H. Bei, G. Eggeler, E.P. George, The influences of temperature and microstructure on the tensile properties of a CoCrFeMnNi high-entropy alloy, *Acta Mater.* 61 (2013) 5743–5755.
- [9] Z. Wu, Y. Gao, H. Bei, Thermal activation mechanisms and Labusch-type strengthening analysis for a family of high-entropy and equiatomic solid-solution alloys, *Acta Mater.* 120 (2016) 108–119.
- [10] Y. Zhang, M.A. Tunes, M.L. Crespiello, F. Zhang, W.L. Boldman, P.D. Rack, L. Jiang, C. Xu, G. Greaves, S.E. Donnelly, L. Wang, W.J. Weber, Thermal stability and irradiation response of nanocrystalline CoCrCuFeNi high-entropy alloy, *Nanotechnology* 30 (2019) 294004.
- [11] A. Poulia, E. Georgatis, A. Lekatou, A.E. Karantzalis, Microstructure and wear behavior of a refractory high entropy alloy, *Int. J. Refract. Met. Hard Mater.* 57 (2016) 50–63.
- [12] M.-H. Chuang, M.-H. Tsai, W.-R. Wang, S.-J. Lin, J.-W. Yeh, Microstructure and wear behavior of $\text{Al}_{x}\text{Co}_{1.5}\text{CrFeNi}_{1.5}\text{Ti}_y$ high-entropy alloys, *Acta Mater.* 59 (2011) 6308–6317.
- [13] Y. Yu, J. Wang, J. Li, J. Yang, H. Kou, W. Liu, Tribological behavior of $\text{AlCoCrFeNi}(\text{Ti}_{0.5})$ high entropy alloys under oil and MACs lubrication, *J. Mater. Sci. Technol.* 32 (2016) 470–476.
- [14] Y.Y. Chen, U.T. Hong, H.C. Shih, J.W. Yeh, T. Duval, Electrochemical kinetics of the high entropy alloys in aqueous environments—a comparison with type 304 stainless steel, *Corros. Sci.* 47 (2005) 2679–2699.
- [15] H. Luo, Z. Li, A.M. Mingers, D. Raabe, Corrosion behavior of an equiatomic CoCrFeMnNi high-entropy alloy compared with 304 stainless steel in sulfuric acid solution, *Corros. Sci.* 134 (2018) 131–139.
- [16] S. Shuang, Z.Y. Ding, D. Chung, S.Q. Shi, Y. Yang, Corrosion resistant nanostructured eutectic high entropy alloy, *Corros. Sci.* 164 (2020), 108315.
- [17] N.A.P.K. Kumar, C. Li, K.J. Leonard, H. Bei, S.J. Zinkle, Microstructural stability and mechanical behavior of FeNiMnCr high entropy alloy under ion irradiation, *Acta Mater.* 113 (2016) 230–244.
- [18] L. Yang, H. Ge, J. Zhang, T. Xiong, Q. Jin, Y. Zhou, X. Shao, B. Zhang, Z. Zhu, S. Zheng, X. Ma, High He-ion irradiation resistance of CrMnFeCoNi high-entropy alloy revealed by comparison study with Ni and 304SS, *J. Mater. Sci. Technol.* 35 (2019) 300–305.
- [19] Y. Lu, H. Huang, X. Gao, C. Ren, J. Gao, H. Zhang, S. Zheng, Q. Jin, Y. Zhao, C. Lu, T. Wang, T. Li, A promising new class of irradiation tolerant materials: $\text{Ti}_2\text{ZrHfV}_{0.5}\text{Mo}_{0.2}$ high-entropy alloy, *J. Mater. Sci. Technol.* 35 (2019) 369–373.
- [20] O.N. Senkov, S.V. Senkova, D.B. Miracle, C. Woodward, Mechanical properties of low-density, refractory multi-principal element alloys of the Cr-Nb-Ti-V-Zr system, *Mater. Sci. Eng. A* 565 (2013) 51–62.
- [21] B. Gorr, M. Azim, H.J. Christ, T. Mueller, D. Schliephake, M. Heilmayer, Phase equilibria, microstructure, and high temperature oxidation resistance of novel refractory high-entropy alloys, *J. Alloys Compd.* 624 (2015) 270–278.
- [22] B. Gorr, F. Müller, M. Azim, H.-J. Christ, T. Müller, H. Chen, A. Kauffmann, M. Heilmayer, High-temperature oxidation behavior of refractory high-entropy alloys: effect of alloy composition, *Oxid. Met.* 88 (2017) 339–349.
- [23] B. Gorr, F. Mueller, H.J. Christ, T. Mueller, H. Chen, A. Kauffmann, M. Heilmayer, High temperature oxidation behavior of an equimolar refractory metal-based alloy 20Nb 20Mo 20Cr 20Ti 20Al with and without Si addition, *J. Alloys Compd.* 688 (2016) 468–477.
- [24] C.P. Lee, C.C. Chang, Y.Y. Chen, J.W. Yeh, H.C. Shih, Effect of the aluminium content of $\text{Al}_{x}\text{CrFe}_{1.5}\text{MnNi}_{0.5}$ high-entropy alloys on the corrosion behaviour in aqueous environments, *Corros. Sci.* 50 (2008) 2053–2060.
- [25] Y.L. Chou, Y.C. Wang, J.W. Yeh, H.C. Shih, Pitting corrosion of the high-entropy alloy $\text{Co}_{1.5}\text{CrFeNi}_{1.5}\text{Ti}_{0.5}\text{Mo}_{0.1}$ in chloride-containing sulphate solutions, *Corros. Sci.* 52 (2010) 3481–3491.
- [26] W. Kai, C.C. Li, F.P. Cheng, K.P. Chu, R.T. Huang, L.W. Tsay, J.J. Kai, Air-oxidation of FeCoNiCr-based quinary high-entropy alloys at 700–900 °C, *Corros. Sci.* 121 (2017) 116–125.
- [27] W. Kai, F.P. Cheng, F.C. Chien, Y.R. Lin, D. Chen, J.J. Kai, C.T. Liu, C.J. Wang, The oxidation behavior of a Ni₂FeCoCrAl_{0.5} high-entropy superalloy in O₂-containing environments, *Corros. Sci.* 158 (2019), 108093.
- [28] W. Kai, F.C. Chien, F.P. Cheng, R.T. Huang, J.J. Kai, C.T. Liu, The corrosion of an equimolar FeCoNiCrMn high-entropy alloy in various CO₂/CO mixed gases at 700 and 950 °C, *Corros. Sci.* 153 (2019) 150–161.
- [29] Y.-J. Hsu, W.-C. Chiang, J.-K. Wu, Corrosion behavior of FeCoNiCrCu_x high-entropy alloys in 3.5% sodium chloride solution, *Mater. Chem. Phys.* 92 (2005) 112–117.
- [30] T. Egami, W. Guo, P.D. Rack, T. Nagase, Irradiation resistance of multicomponent alloys, *Metall. Mater. Trans. A* 45 (2013) 180–183.
- [31] C. Xiang, J. Wang, H. Fu, E.H. Han, Z. Zhang, Corrosion behavior of several high-entropy alloys in high temperature high pressure water, *J. Chin. Soc. Corros. Prot.* 36 (2016) 107–112.
- [32] Y.-x. Liu, C.-q. Cheng, J.-l. Shang, R. Wang, P. Li, J. Zhao, Oxidation behavior of high-entropy alloys $\text{Al}_{x}\text{CoCrFeNi}$ ($x=0.15, 0.4$) in supercritical water and comparison with HR3C steel, *Trans. Nonferrous Met. Soc. China* 25 (2015) 1341–1351.
- [33] C. Xiang, H.M. Fu, Z.M. Zhang, E.H. Han, H.F. Zhang, J.Q. Wang, G.D. Hu, Effect of Cr content on microstructure and properties of $\text{Mo}_{0.5}\text{VNbTiCr}_x$ high-entropy alloys, *J. Alloys Compd.* 818 (2020), 153352.
- [34] Z. Zhang, E.-H. Han, C. Xiang, Irradiation behaviors of two novel single-phase bcc-structure high-entropy alloys for accident-tolerant fuel cladding, *J. Mater. Sci. Technol.* 84 (2021) 230–238.
- [35] Y.Y. Chen, T. Duval, U.T. Hong, J.W. Yeh, H.C. Shih, L.H. Wang, J.C. Oung, Corrosion properties of a novel bulk $\text{Cu}_{0.5}\text{NiAlCoCrFeSi}$ glassy alloy in 288 degrees C high-purity water, *Mater. Lett.* 61 (2007) 2692–2696.
- [36] G. Lei, R. Xie, H. Huang, R. Liu, Q. Huang, J. Li, Y. Zhou, C. Li, Q. Lei, Q. Deng, Y. Wang, C. Wang, W. Zhang, L. Yan, M. Tang, The effect of He bubbles on the swelling and hardening of UNS N10003 alloy, *J. Alloys Compd.* 746 (2018) 153–158.
- [37] W.B. Liu, J.H. Zhang, Y.Z. Ji, L.D. Xia, H.P. Liu, D. Yun, C.H. He, C. Zhang, Z. G. Yang, Comparative study of He bubble formation in nanostructured reduced activation steel and its coarsen-grained counterpart, *J. Nucl. Mater.* 500 (2018) 213–219.
- [38] J.C. Haley, S.A. Briggs, P.D. Edmondson, K. Sridharan, S.G. Roberts, S. Lozano-Perez, K.G. Field, Dislocation loop evolution during in-situ ion irradiation of model FeCrAl alloys, *Acta Mater.* 136 (2017) 390–401.
- [39] A. Etienne, M. Hernández-Mayoral, C. Genevois, B. Radiguet, P. Pareige, Dislocation loop evolution under ion irradiation in austenitic stainless steels, *J. Nucl. Mater.* 400 (2010) 56–63.
- [40] D.H. Lister, R.D. Davidson, E. McAlpine, The mechanism and kinetics of corrosion product release from stainless-steel in lithiated high-temperature water, *Corros. Sci.* 27 (1987) 113–140.
- [41] J. Robertson, The mechanism of high-temperature aqueous corrosion of stainless-steels, *Corros. Sci.* 32 (1991) 443–465.
- [42] B. Stellwag, The mechanism of oxide film formation on austenitic stainless steels in high temperature water, *Corros. Sci.* 40 (1998) 337–370.
- [43] X. Ren, K. Sridharan, T.R. Allen, Corrosion behavior of alloys 625 and 718 in supercritical water, *Corrosion* 63 (2007) 603–612.
- [44] D.D. Macdonald, Theory of steady-state passive films, *J. Electrochem. Soc.* 137 (1990) 2395.
- [45] L. Marchetti, S. Perrin, F. Jambon, M. Pijolat, Corrosion of nickel-base alloys in primary medium of pressurized water reactors: new insights on the oxide growth mechanisms and kinetic modelling, *Corros. Sci.* 102 (2016) 24–35.
- [46] J. Zhang, Y. Hu, J. Huang, L. Tu, M. Yao, B. Zhou, The corrosion resistance of $\text{Zr}-0.75\text{Sn}-0.2\text{Fe}-x\text{Cu}-x\text{Ge}$ alloys in 360 °C lithiated water, *Corros. Sci.* 111 (2016) 132–138.
- [47] M. Yao, J. Huang, K. Hou, H. Zhao, X. Liang, J. Zhang, B. Zhou, Q. Li, Analysis of blister-like morphology on the oxide film of $\text{Zr}-\text{Nb}$ alloy corroded in lithiated water, *Corros. Sci.* 178 (2021), 109075.
- [48] T. Kim, J. Kim, K.J. Choi, S.C. Yoo, S. Kim, J.H. Kim, Phase transformation of oxide film in zirconium alloy in high temperature hydrogenated water, *Corros. Sci.* 99 (2015) 134–144.
- [49] B.X. Huang, K. Wang, J.S. Church, Y.-S. Li, Characterization of oxides on niobium by Raman and infrared spectroscopy, *Electrochim. Acta* 44 (1999) 2571–2577.
- [50] A.C. Alves, F. Wenger, P. Ponthiaux, J.P. Celis, A.M. Pinto, L.A. Rocha, J.C. S. Fernandes, Corrosion mechanisms in titanium oxide-based films produced by anodic treatment, *Electrochim. Acta* 234 (2017) 16–27.
- [51] K. Kruska, S. Lozano-Perez, D.W. Saxeby, T. Terachi, T. Yamada, G.D.W. Smith, Nanoscale characterisation of grain boundary oxidation in cold-worked stainless steels, *Corros. Sci.* 63 (2012) 225–233.
- [52] L. Dong, Q. Peng, E.-H. Han, W. Ke, L. Wang, Stress corrosion cracking in the heat affected zone of a stainless steel 308L-316L weld joint in primary water, *Corros. Sci.* 107 (2016) 172–181.
- [53] S. Hu, Y. Mao, X. Liu, E.-H. Han, H. Hänninen, Intergranular corrosion behavior of low-chromium ferritic stainless steel without Cr-carbide precipitation after aging, *Corros. Sci.* 166 (2020), 108420.
- [54] P. Deng, Q. Peng, E.-H. Han, W. Ke, C. Sun, Z. Jiao, Effect of irradiation on corrosion of 304 nuclear grade stainless steel in simulated PWR primary water, *Corros. Sci.* 127 (2017) 91–100.
- [55] S. Perrin, L. Marchetti, C. Duhamel, M. Sennour, F. Jomard, Influence of irradiation on the oxide film formed on 316 L stainless steel in PWR primary water, *Oxid. Met.* 80 (2013) 623–633.
- [56] Y. Chimi, Y. Kitsunai, S. Kasahara, K. Chatani, M. Koshiishi, Y. Nishiyama, Correlation between locally deformed structure and oxide film properties in austenitic stainless steel irradiated with neutrons, *J. Nucl. Mater.* 475 (2016) 71–80.
- [57] S.S. Raiman, G.S. Was, Accelerated corrosion and oxide dissolution in 316L stainless steel irradiated in situ in high temperature water, *J. Nucl. Mater.* 493 (2017) 207–218.
- [58] X. Lin, Q. Peng, J. Mei, E.-H. Han, W. Ke, L. Qiao, Z. Jiao, Corrosion of phase and phase boundary in proton-irradiated 308L stainless steel weld metal in simulated PWR primary water, *Corros. Sci.* (2019), 108401.
- [59] Z. Jiao, G.S. Was, Novel features of radiation-induced segregation and radiation-induced precipitation in austenitic stainless steels, *Acta Mater.* 59 (2011) 1220–1238.
- [60] V. Markelov, V. Novikov, A. Shevyakov, A. Gusev, A. Obukhov, Preliminary irradiation effect on corrosion resistance of zirconium alloys, *Zirconium in the Nuclear Industry: 18th International Symposium* (2018).